

Hyperspectral imaging of plasmonic nanostructures with nanoscale resolution

M. V. Bashevoy,¹ F. Jonsson,¹ K. F. MacDonald,^{1*} Y. Chen,² and N. I. Zheludev¹

¹ Optoelectronics Research Centre, University of Southampton, Southampton, SO17 1BJ, United Kingdom

² Rutherford Appleton Laboratory, Didcot, Oxfordshire, OX11 0QX, United Kingdom

Corresponding author: kfm@orc.soton.ac.uk

<http://www.nanophotonics.org.uk/niz/>

Abstract: We report on the first realization of a hyperspectral imaging technique for surface plasmon polaritons on metallic nanostructures. The technique uses a scanning electron beam and allows for simple visualization of light emission from decoupled plasmons, providing information on decay lengths and feature sizes with nanometer resolution.

©2007 Optical Society of America

OCIS codes: (240.6680) Surface plasmons; (250.5403) Plasmonics.

References and Links

1. S. A. Maier, *Plasmonics: Fundamentals and Applications* (Springer, New York, 2007).
2. V. M. Shalaev and S. Kawata, eds. *Nanophotonics with Surface Plasmons* (Elsevier, Amsterdam, 2007)
3. W. L. Barnes, A. Dereux, and T. W. Ebbesen, "Surface plasmon subwavelength optics", *Nature* **424**, 824-830 (2003).
4. A. V. Zayats, I. I. Smolyaninov, and A. A. Maradudin, "Nano-optics of surface plasmon polaritons," *Phys. Rep.* **408**, 131-314 (2005).
5. R. Zia, J. A. Schuller, A. Chandran, and M. L. Brongersma, "Plasmonics: the next chip-scale technology," *Materials Today* **9**, 20-27 (2006).
6. M. V. Bashevoy, F. Jonsson, A. V. Krasavin, and N. I. Zheludev, Y. Chen, M. I. Stockman, "Generation of Traveling Surface Plasmon Waves by Free-Electron Impact," *Nano Lett.* **6**, 1113-1115 (2006).
7. J. T. van Wijngaarden, E. Verhagen, and A. Polman, C. E. Ross, H. J. Lezec and H. A. Atwater, "Direct imaging of propagation and damping of near-resonance surface plasmon polaritons using cathodoluminescence spectroscopy," *Appl. Phys. Lett.* **88**, 221111 (2006).
8. R. O. Green, M. L. Eastwood, C. M. Sarture, T. G. Chrien, M. Aronsson, B. J. Chippendale, J. A. Faust, B. E. Pavri, C. J. Chovit, M. S. Solis, M. R. Olah, and O. Williams, "Imaging spectroscopy and the Airborne Visible Infrared Imaging Spectrometer (AVIRIS)," *Remote Sens. Environ.* **65**, 227-248 (1998).
9. E. D. Palik, ed. *Handbook of Optical Constants of Solids* (Academic Press, Orlando, 1985).
10. A. V. Krasavin, K. F. MacDonald and N. I. Zheludev, "Active Plasmonics," in *Nanophotonics with Surface Plasmons*, V. M. Shalaev and S. Kawata, ed. (Elsevier, Amsterdam, 2007).

Surface plasmon polariton (SPP) waves are electromagnetic field oscillations propagating at metal-dielectric interfaces, which currently attract considerable interest in the fields of optics and surface science due to their ability to concentrate and channel radiation in the visible and near-infra-red spectral ranges using sub-wavelength structures [1-5]. In particular, SPP's are seen to have great potential for application as information carriers in highly integrated photonic devices and next-generation computer processor architectures.

To obtain phase matching between the wave vectors of light and SPP waves at a metallic interface, the excitation of SPP's is traditionally performed using coupling structures such as prisms or gratings. However, it has recently been demonstrated that a focused free-electron beam impacting on an unstructured metal surface can act as an efficient, broadband, nano-scale SPP source [6,7]. This SPP generation technique has several advantages over traditional methods, such as high spatial localization (significantly below the diffraction limit of light), a high degree of source mobility, and the elimination of (typically large) coupling structures.

Here we report on the development and capabilities of a new 'hyperspectral' imaging (HSI) technique for the visualization of plasmon excitations in metal nanostructures, based on the functionality of the electron beam SPP source in a scanning electron microscope (SEM).

A pixel in a conventional image typically contains information on the intensities of three color channels: red, green, and blue. In HSI (a concept well known in geographic and atmospheric research [8]) each sampled pixel contains an entire spectrum of data – the intensities of hundreds if not thousands of individual wavelength channels. In the realization reported here, the hyperspectral image is formed by scanning a structure with a focused electron beam and synchronously recording the light emission spectrum from the decoupling of the plasmons generated at every pixel (Fig. 1(a)), in the present case sampling 1024 wavelengths between 350 and 1150 nm. This decoupling can occur either through scattering at random surface imperfections or, as in the experiments reported below, via a nearby purposely engineered decoupling grating. The HSI technique generates a three-dimensional ‘data cube’ (Fig. 1(b)) with two spatial axes, defining the co-ordinates of electron beam injection points in the sample plane, and a spectral axis. This cube can be ‘mined’ in a number of ways to obtain, for example, single-wavelength spatial intensity distributions of plasmonic emission, point spectra, and wavelength-specific linear emission intensity profiles (from which, under certain conditions, SPP decay lengths can be derived).

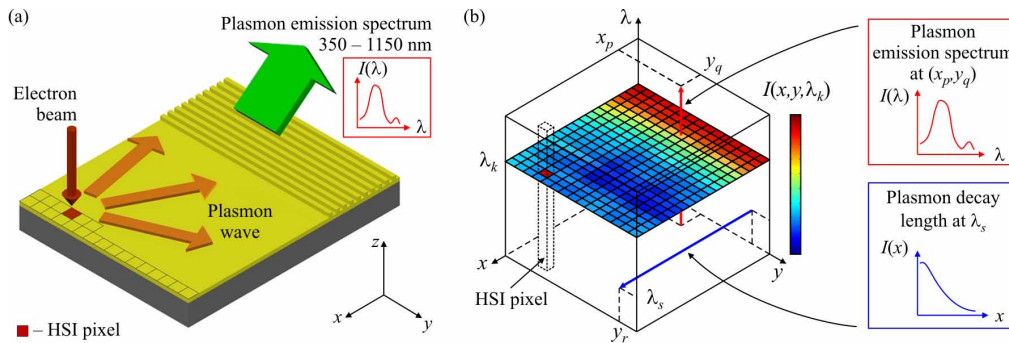


Fig. 1. (a) The hyperspectral imaging concept illustrated for a grating on a gold film. At each electron beam injection point in the sample (x - y) plane, i.e. each image pixel, the entire emission spectrum from decoupled surface plasmons is sampled simultaneously at a number of discrete wavelengths λ_k . (b) The data cube generated can be mined to produce single-wavelength spatial intensity distributions of plasmonic emission (x - y planes), point spectra (vertical lines), and wavelength-specific linear emission intensity profiles (horizontal lines).

The spectra obtained in HSI are determined primarily by the material properties and nanoscale topography of the nanostructure under investigation and the geometry of the light-collection system. To illustrate this, experiments were performed on gold grating samples using wide- and narrow-angle parabolic light-collection mirrors to direct decoupled light out of the SEM chamber, via a fused silica window, to a spectrometer (Fig. 2).

Gratings facilitate SPP decoupling to light by compensating for the mismatch between their wave vectors with an integer multiple of the grating vector $k_G = 2\pi/a$, where a is the grating period. The wavelength dependence of the decoupling angle θ is described by the equation

$$\text{Re}\{k_{SPP}(\omega)\} - nk_G = (\omega/c) \sin(\theta(\omega)), \quad (1)$$

where n is a positive integer and $k_{SPP}(\omega)$ is the SPP wave vector, which at a metal/vacuum interface depends on the complex permittivity $\varepsilon(\omega)$ of the metal according to the equation

$$\text{Re}\{k_{SPP}(\omega)\} = \frac{\omega}{c} \text{Re}\left\{\left(\frac{\varepsilon(\omega)}{1 + \varepsilon(\omega)}\right)^{1/2}\right\}.$$

Only wavelengths decoupled at angles within the light-collection system's 'acceptance window' (defined by the mirror's dimensions and its position relative to the sample) can be detected by the spectrometer. For the purposes of the present demonstrations, a comparatively small wide-angle mirror located just 1 mm above the sample provided an acceptance window extending from $\theta_a = -70^\circ$ to $\theta_b = 30^\circ$ (Fig. 2(a)), while a larger narrow-angle mirror located ~ 5 cm to one side of the sample provided a window between $\theta_a = -82^\circ$ and $\theta_b = -67^\circ$ (Fig. 2(b)).

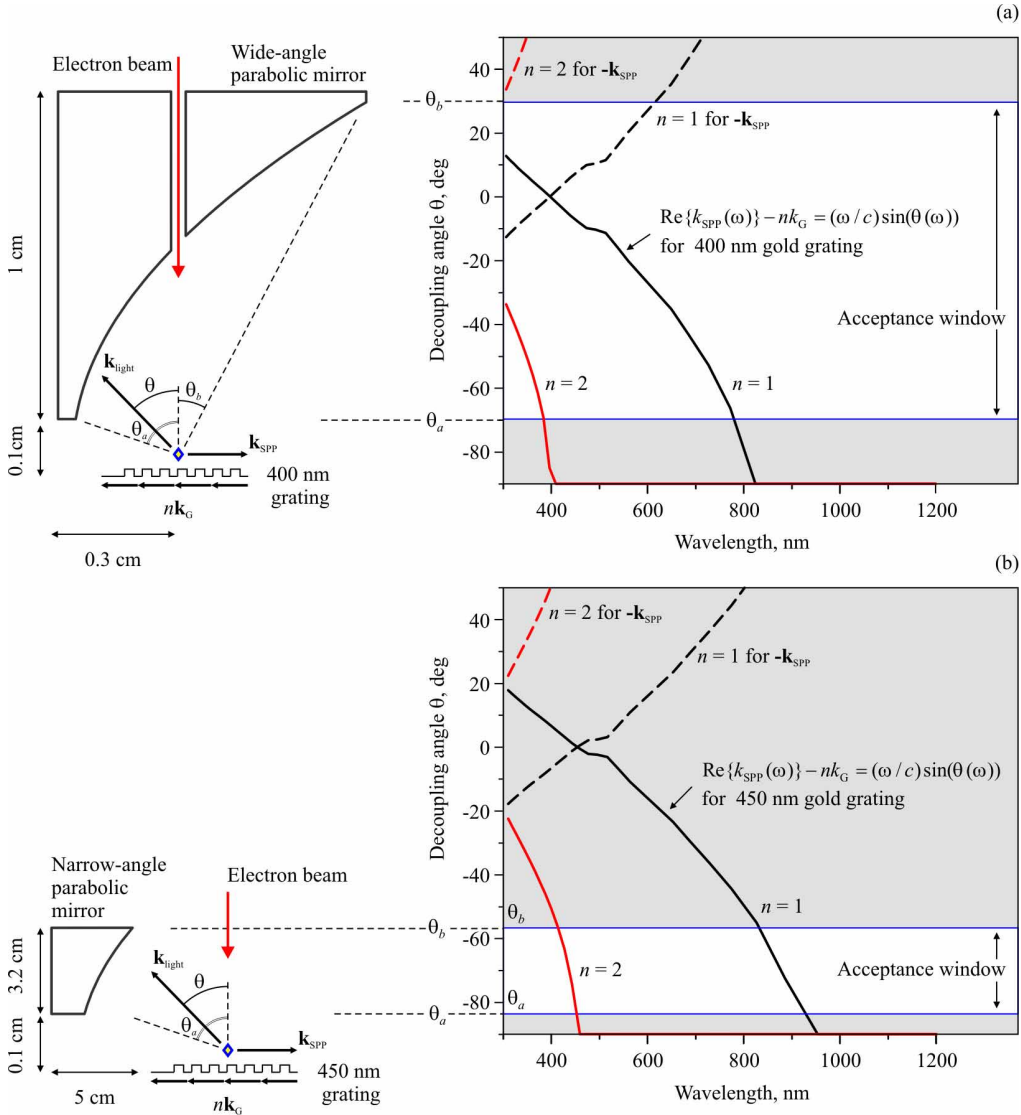


Fig. 2. Hyperspectral imaging light-collection geometries and angular decoupling diagrams for the gratings imaged in each configuration. (a) The wide-angle light-collection geometry with its acceptance window, $-70^\circ < \theta < 30^\circ$, mapped onto the 400 nm period grating's decoupling diagram. (b) The narrow-angle collection geometry with its acceptance window, $-82^\circ < \theta < -67^\circ$, mapped onto the 450 nm period grating's decoupling diagram. (Note that the two mirrors are drawn to different scales to achieve the correct schematic mapping of their acceptance windows onto the decoupling diagrams.)

The samples studied were 400 and 450 nm period gratings, each comprising thirty lines with a height of 50 nm (Fig.'s 3(a) and 4(a)), prepared by electron beam lithography on 200 nm thick evaporated gold films on silicon (a sufficient film thickness to exclude any influence from SPP's excited on the metal/substrate interface). The wide-angle mirror was employed to image the 400 nm grating sample and the narrow-angle mirror to image the 450 nm sample. Mapping the mirrors' angular acceptance windows onto the gratings' decoupling diagrams (plots of decoupling angle vs. wavelength, calculated using optical constants for gold from [9]) as shown in Fig. 2, illustrates the effect that light-collection geometry has on recorded spectra: Both gratings generate first- ($n = 1$) and second-order ($n = 2$) decoupled light within the wavelength range of the spectrometer. With the narrow-angle mirror the two orders are expected to generate separate narrow signal peaks at different wavelengths, but with the wide-angle mirror there can be no such separation because the spectral range of the first-order extends to the lower limit of the detection range (completely overlapping the second order). However, at the expense of angular resolution, the wide-angle mirror offers a smaller minimum working distance for the SEM (enabling higher resolution imaging), and is found in practice to provide a light-collection efficiency up to three orders of magnitude higher than the narrow-angle mirror (allowing for shorter imaging times and the use of lower beam currents). When the electron beam injection point lies within a grating (rather than to one side of it), both the positive and negative directions of k_{SPP} must be considered. In the narrow-angle configuration, the acceptance window is such that light decoupled from plasmons with negative k_{SPP} values (dashed decoupling curves in Fig. 2) cannot be detected. However, in the wide-angle configuration, first-order decoupling from SPP's with negative k_{SPP} values contributes to the detected signal at wavelengths up to ~ 620 nm.

Hyperspectral imaging was performed on rectangular sample areas encompassing, in each case, the grating and an adjacent area of unstructured gold surface (Fig.'s 3(a) and 4(a)), using a 20 kV electron beam with a spot size of ~ 10 nm. In the wide-angle configuration the pixel size (distance between adjacent electron beam injection points) was $0.6 \mu\text{m}$, and the dwell time per pixel was 2 s. In the narrow-angle configuration, injection point spacings of $0.5 \mu\text{m}$ in the x -direction and $2.4 \mu\text{m}$ in the y -direction were used (larger in the y -direction because all sample cross-sections parallel to x are the same), with a dwell time of 5 s. By subtracting background emission spectra for areas of unstructured gold (far outside those shown in Fig.'s 3(a) and 4(a)) from the HSI spectra, normalized spectra relating only to emission from SPP decoupling at the gratings were obtained [6]. This normalization aims to eliminate luminescence (from the recombination of d -band holes created by the electronic excitation), dipole radiation (from the coming together of incident electrons and their mirror images in the sample), light decoupled from SPP's by scattering at random surface imperfections, and fluorescence from any residual contaminants on the sample.

By 'slicing' the normalized hyperspectral data cube at a fixed wavelength (such as λ_k in Fig. 1(b)), one obtains the spatial intensity distribution of light decoupled from SPP's at that wavelength, as a function of electron beam injection coordinate. Sequences of such images reveal the evolution of plasmon emission over the sampled area as a function of wavelength, as illustrated in Fig.'s 3(b-d) and 4(b-d) (where distributions are averaged over 7 nm wavelength intervals to reduce noise): For both gratings there are ranges, exemplified by distributions at 1030-1037 nm (Fig.'s 3(d) and 4(d)), where there is little or no emission, indicating either that SPP's are not generated in this range or that they do not interact with the grating; Both also have highly resonant ranges, illustrated at 617-624 nm for the 400 nm grating (Fig. 3(c)) and 835-842 nm for the 450 nm grating (Fig. 4(c)), where the gratings efficiently decouple SPP's to optical radiation. For the 450 nm grating there is a range, exemplified by the distribution at 730-737 nm in Fig. 4(b), where the *recorded* signal falls below the background level, indicating that the grating inhibits background emission (most likely from SPP scattering) at angles within the narrow-angle mirror's acceptance window. The inset to Fig. 3(c) demonstrates the higher resolution capability of the wide-angle collection geometry: In this image (obtained with a 30×30 nm pixel size and 0.5 s dwell time) the individual grating lines can be identified in the emission pattern.

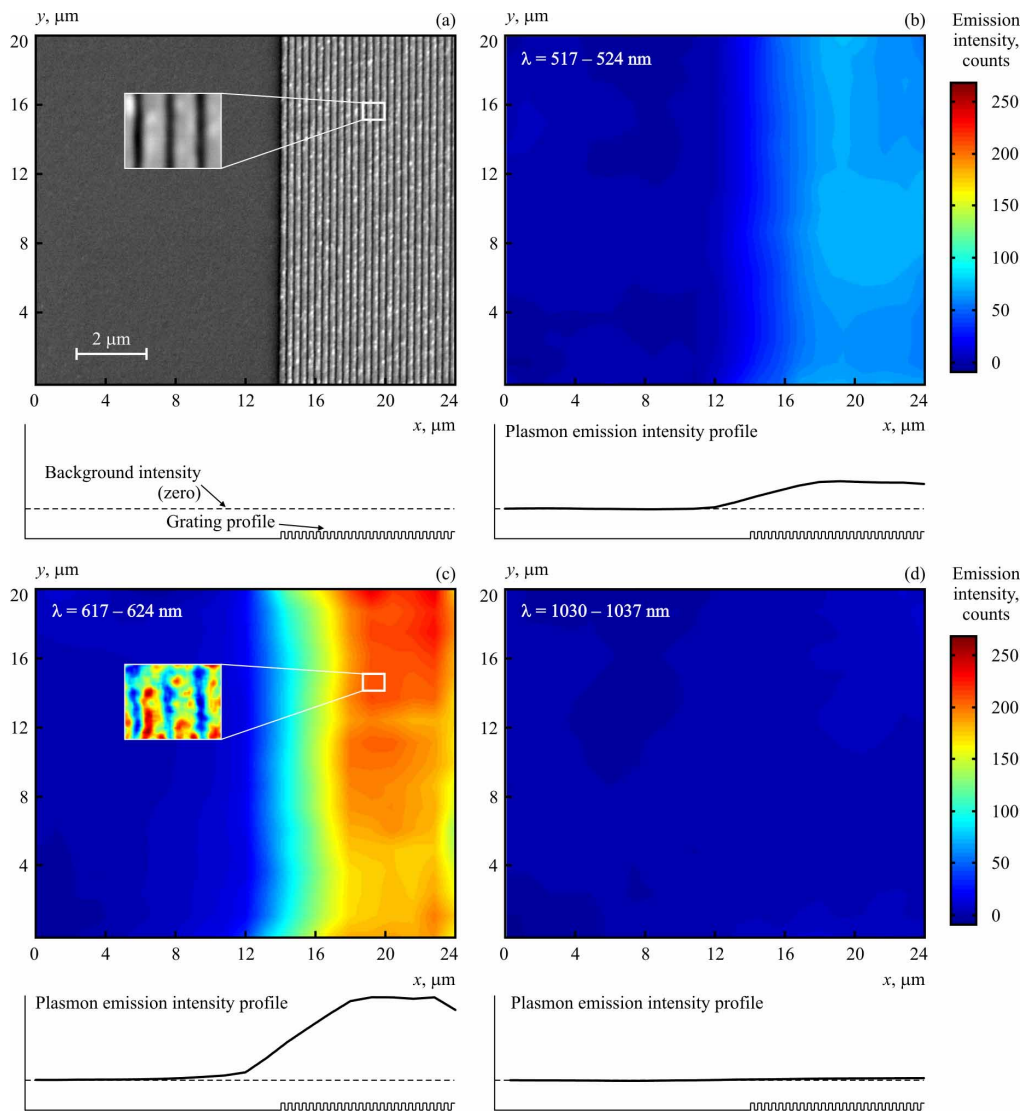


Fig. 3. (Movie: 3.1 MB) Hyperspectral imaging of the 400 nm gold grating sample with the wide-angle parabolic light-collection mirror. (a) Secondary electron image of the sample area, encompassing grating and adjacent unstructured gold film, which was imaged in hyperspectral mode. (b, c and d) Spatial plasmonic emission intensity distributions obtained by slicing the hyperspectral data cube in the x - y plane (averaged over 7 nm wavelength intervals), with corresponding average emission intensity profiles along the x direction: (b) 517-524 nm, where the grating is weakly resonant and plasmon decoupling efficiency is relatively poor; (c) 617-625 nm, where the grating is resonant and efficiently decouples plasmons to optical radiation; (d) 1030-1037 nm, where emission is negligible. The insets to (a) shows a high-resolution image of a small part of the grating. The inset to (c) shows the corresponding emission intensity distribution at 617-625 nm, wherein the grating structure is resolved.

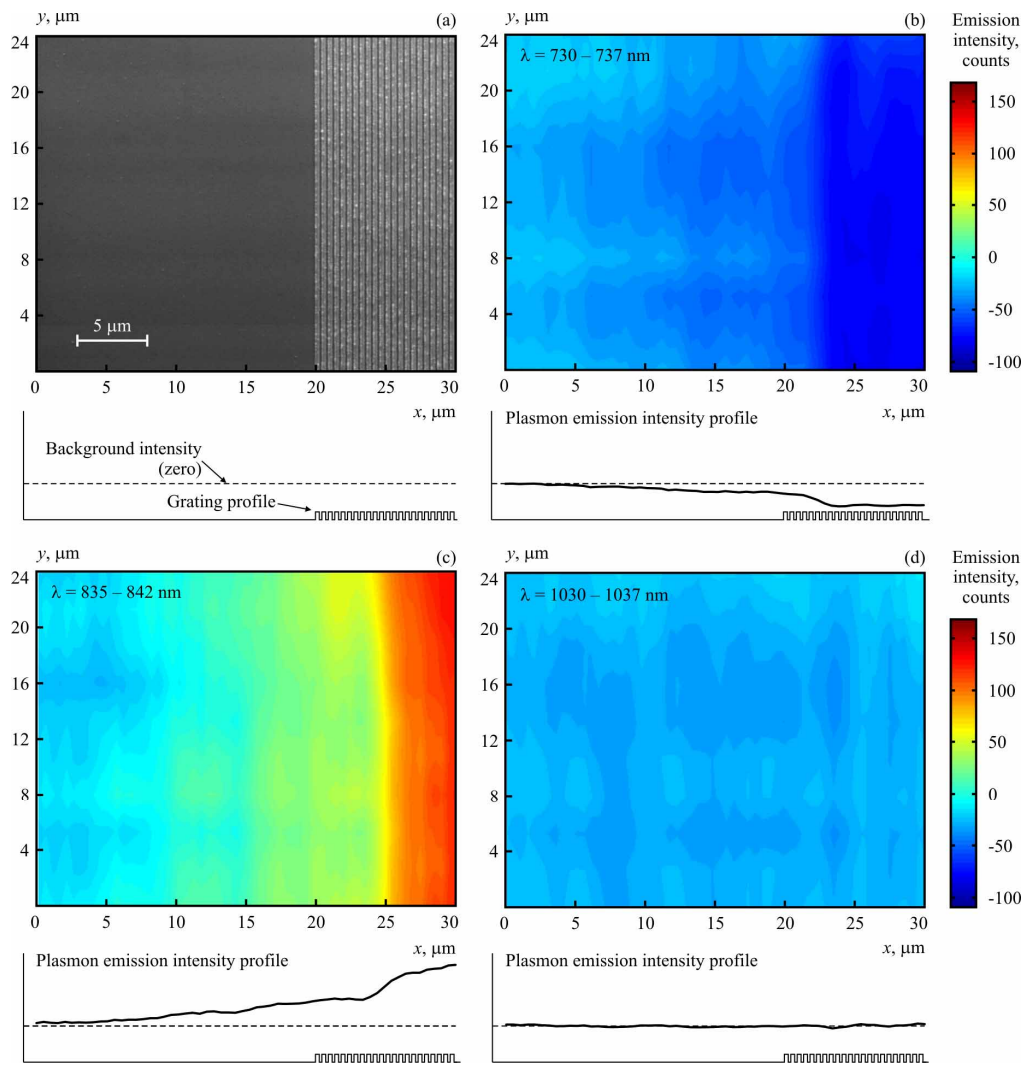


Fig. 4. (Movie: 3.5 MB) Hyperspectral imaging of the 450 nm gold grating sample with the narrow-angle parabolic light-collection mirror. (a) Secondary electron image of the sample area, encompassing grating and adjacent unstructured gold film, which was imaged in hyperspectral mode. (b, c and d) Spatial plasmonic emission intensity distributions obtained by slicing the hyperspectral data cube in the x - y plane (averaged over 7 nm wavelength intervals), with corresponding average emission intensity profiles along the x direction: (b) 730-737 nm, where the grating inhibits background emission at angles within the mirror's acceptance window.; (c) 835-842 nm, where the grating is resonant and efficiently decouples plasmons to optical radiation; (d) 1030-1037 nm, where emission is negligible.

The HSI data cube can also be mined for information on decoupled light spectra and SPP decay lengths. By plotting intensity data along a line of fixed spatial coordinate in the cube, such as the vertical line at (x_p, y_q) in Fig. 1(b), one obtains the decoupling emission spectrum (convoluted with the acceptance window of the light-collection geometry) for electron beam injection (SPP generation) at that point. By plotting intensity data along a line within a fixed-wavelength x - y plane, such as the horizontal line at (y_r, λ_s) in Fig. 1(b), one obtains a linear emission intensity profile. If the line selected is perpendicular to the edge of a decoupling structure on the sample surface, then the SPP decay length at λ_s can be derived from an exponential fit to the intensity profile. Fig. 5 illustrates such analyses for the present cases.

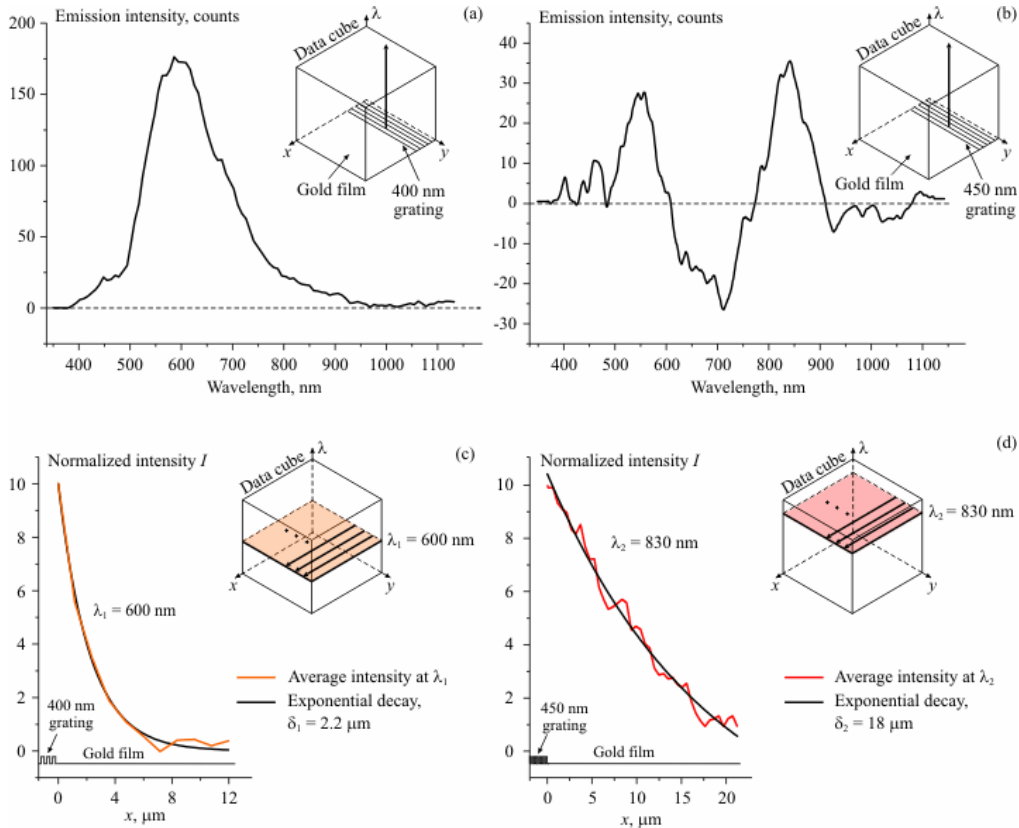


Fig. 5. Single point spectra and surface plasmon decay lengths extracted from the hyperspectral imaging data cubes. Single-pixel spectra for points within: (a) the 400 nm period grating, recorded with the wide-angle light-collection geometry; (b) the 450 nm grating, recorded with the narrow-angle geometry. Linear emission intensity profiles along the x -direction (perpendicular to the grating lines), averaged over all values of y , for: (c) the 400 nm grating sample at $\lambda_1 = 600$ nm; (d) the 450 nm grating sample at $\lambda_2 = 830$ nm. Distances along x are measured relative to the edge of the gratings. Plasmon decay lengths δ are determined from exponential fittings to the data. The bold arrows in each figure's inset show the line(s) along which data is extracted from the cube to obtain the corresponding curve.

Figures 5(a) and (b) show spectra for single-pixel points within the 400 and 450 nm gratings respectively. Fig. 5(a) shows a single broad emission peak for the 400 nm grating, centered at ~ 600 nm. This may appear inconsistent with Fig. 2(a), which indicates that the wide-angle light-collection geometry is capable of detecting first-order ($n = 1$) SPP decoupling at wavelengths down to the 350 nm lower limit of the spectrometer. However, mappings such as those shown in Fig. 2 must be interpreted with care, in particular because Eq. (1) says nothing about the *efficiency* of SPP decoupling and scattering processes, which are complex wavelength-dependent functions of grating period, line-width and line-height that can only be analyzed numerically [10]. Neither does it take into account the spectrum of the electron beam SPP source, or the plasmon waves' decay lengths $\delta = [2\text{Im}\{k_{\text{SPP}}(\omega)\}]^{-1}$. Indeed for wavelengths shorter than ~ 510 nm, the SPP decay length is shorter than the period of either grating used in the present study, so grating-mediated decoupling is not possible.

In accordance with Fig. 2, the narrow-angle geometry records a narrow peak in the near infra-red range, corresponding to the first ($n = 1$) decoupling order (Fig. 5b)). For the reasons of poor short-wavelength decoupling efficiency described above, the predicted second-order ($n = 2$) peak at ~ 420 nm is not observed, however a peak centered at ~ 550 nm is recorded.

This emission is most likely to result from the scattering of SPP's to light by the lines of the grating. As noted above, the scattering efficiency is a complex function of wavelength and grating geometry, however in general, while it may be as low as a few percent, it increases significantly as line-width deviates from $a/2$ (they are nearer $3a/4$ in the present cases) and as grating height exceeds $\sim 0.07\lambda$ (i.e. as wavelength decreases below ~ 710 nm in the present cases) [10]. As noted above (see Fig. 4(b)), there is a wavelength range, shown in Fig. 5(b) to be centered at ~ 700 nm, over which the 450 nm grating inhibits background SPP scattering emission within the narrow-angle mirror's acceptance window.

Figures 5(c) and 5(d) show linear emission intensity profiles along the x -direction (perpendicular to the grating lines), averaged over all values of y , for the 400 nm grating sample at $\lambda_1 = 600$ nm, and for the 450 nm sample at $\lambda_2 = 830$ nm. SPP decay lengths of $\delta_1 = 2.2$ μm (at 600 nm), and $\delta_2 = 18$ μm (at 830 nm) are obtained from exponential fittings to this data. These may be compared with theoretical values of $\delta_{600} = 4.3$ μm , and $\delta_{830} = 53$ μm (where subscripts denote wavelength), calculated for an ideal gold/vacuum interface using optical constants for gold from [9]. The experimental lengths are shorter primarily because of losses due to scattering at random surface imperfections on the real gold film.

In conclusion, we have performed the first demonstration of a hyperspectral imaging technique for the visualization of surface plasmon polaritons in metallic structures. The technique employs the electron beam of a scanning electron microscope as a broadband plasmon source for quantitative, single-scan studies of light emission from plasmonic nanostructures, which can yield spatial emission intensity distributions, single-point emission spectra, and plasmon decay lengths with the nanoscale resolution of the electron microscope. Demonstrative studies have illustrated the relative merits of wide- and narrow-angle light-collection geometries, and have shown that results must always be interpreted with due consideration for the dielectric properties of sample media and the assorted modes of plasmon interaction with surface features. Possible applications of this technique include the visualization of plasmon modes in single nanoparticles, particle dimers or clusters, and metamaterial nanostructures.

The authors would like to acknowledge the support of the Engineering and Physical Sciences Research Council (EPSRC), United Kingdom, and the EU STRP-016881 Project SPANS.